Research Square

Preprints are preliminary reports that have not undergone peer review.
They should not be considered conclusive, used to inform clinical practice,
or referenced by the media as validated information.

Weakly Nonlinear Analysis of Thermal Convection in an Oldroyd-B Fluid Saturating an Anisotropic Bidispersive Porous Medium

SMILE BANSAL

Thapar Institute of Engineering & Technology

SAPNA SHARMA

sapna.sharma@thapar.edu

Thapar Institute of Engineering & Technology

Research Article

Keywords: Thermal convective instability, Weakly nonlinear analysis, Anisotropic bidispersive porous medium, Oldroyd-B uid, Heat transfer

Posted Date: September 29th, 2026

DOI: https://doi.org/10.21203/rs.3.rs-11059508/v1

License: This work is licensed under a Creative Commons Attribution 4.0 International License.
Read Full License

Additional Declarations: No competing interests reported.

Version of Record: A version of this preprint was published at Theoretical and Computational Fluid Dynamics on November 15th, 2026. See the published version at https://doi.org/10.1007/s00162-026-00803-2.

Weakly Nonlinear Analysis of Thermal Convection in an Oldroyd-B Fluid Saturating an Anisotropic Bidispersive Porous Medium

Smile Bansal, Sapna Sharma*

Department of Mathematics, Thapar Institute of Engineering and Technology, Patiala-147001, India

Abstract

To capture the inherent structural heterogeneity of real-world porous media, the current study investigates weakly nonlinear evolution of thermal convection in an Oldroyd-B fluid saturating a horizontal bidispersive porous medium (BDPM). Owing to the preferential pore orientation and hierarchical geometric stratification frequently observed in naturally occurring BDPM, anisotropic permeability is incorporated in both the macro- and micro-pore phases, while a modified Darcy–Oldroyd model is employed to govern the flow dynamics in each phase. To capture both the onset of thermal convection and subsequent evolution of system in the vicinity of critical regimes, a finite-amplitude Ginzburg–Landau equation is derived via multiple-scales expansion, thereby enabling a systematic investigation of the stability and heat transfer characteristics of the system beyond the linear thresholds. Our findings reveal that the directional dependence of permeability in both the macro and micro pore phases raise the critical Rayleigh number by approximately 330.26% relative to the isotropic case, whereas the micro pore anisotropy alone augments it by only 0.84%. Moreover, the time-averaged rate of heat transfer in an anisotropic BDPM exhibits a significant enhancement of approximately 45.60% due to the viscoelastic effects associated with the Oldroyd-B fluid rheology, relative to its Newtonian limit. Furthermore, it is observed that the Oldroyd-B fluid exhibits an earlier and considerably sharper transition towards the convective regime, demonstrating an accelerated transient development of convective heat transport.

Keywords: Thermal convective instability, Weakly nonlinear analysis, Anisotropic bidispersive porous medium, Oldroyd-B fluid, Heat transfer

1. Introduction

In recent years, the phenomenon of thermal convection within a bidispersive porous medium (BDPM) has garnered tremendous attention owing to its wide relevance in a diverse range of natural and industrial systems such as catalytic reactors, thermal energy storage, heat exchangers, geothermal energy reservoirs, fibrous insulation, catalyst beds, wherein the porous matrix is in-

*Corresponding author
Email address: sapna.sharma@thapar.edu

herently structured at two distinct length scales [1, 2]. Unlike conventional (monodisperse) porous media, wherein transport is governed by a single macroscopic permeability, a BDPM is composed of clusters of large particles, referred to as macropores, within which relatively smaller voids, termed micropores, are embedded, giving rise to two distinct velocity and pressure fields that interact through a momentum transfer mechanism [3, 4]. This dual-porosity structure fundamentally alters the onset and evolution of buoyancy-driven convection relative to classical Darcy-Benard configurations, motivating a wide spectrum of theoretical and computational work aimed at characterizing the stability thresholds and heat transfer performance of such systems.

Building upon this, the onset of thermal convection in a horizontal layer uniformly heated from below was examined using a modified Darcy-Brinkman model in a BDPM [5]. To examine the system's stability at the critical thresholds and in the vicinity of these critical regimes, linear and weakly nonlinear analysis of Brinkman-Benard convection was conducted in a BDPM [6]. The study demonstrated that micro and macropores in the medium exert a substantial influence on the stability and heat transport characteristics. Further, the impact of viscous dissipation was examined on thermal convection in a BDPM, confirming the validity of the principle of exchange of stabilities [7]. Subsequently, Soret-driven thermosolutal convection was analyzed in a BDPM, revealing that the interphase momentum transfer coefficient plays a significant role in driving the system's stability [8]. Notably, this study conducted both the linear and weakly nonlinear stability analysis by deriving the cubic Ginzbug-Landau equation and demonstrated a critical interplay between the buoyant forces and the heat transfer characteristics of the system. Thereafter, numerous studies investigated thermal convective instability in a BDPM under various configurations [9–15]. However, these studies have predominantly considered the Newtonian fluid rheology, wherein the stress varies linearly with the strain rate. Such an assumption, while analytically convenient, often fails to capture the true convective behavior of a wide class of fluids encountered frequently in various industrial, biological, and geophysical environments, such as polymer melts, drilling muds, blood flow in the microvasculature, and many more.

In various practical applications such as enhanced oil recovery, groundwater remediation, and biomedical transport through vascular and tissue networks, the fluids saturating BDPM are frequently non-Newtonian in nature, exhibiting pronounced viscoelastic rheology arising from polymer additives, suspended macromolecular content, or intrinsic biofluid microstructure [16, 17]. To account for such viscoelastic effects within a BDPM, the impact of Oldroyd B fluid on thermal convective instability was examined, delineating the crucial role of associated relaxation and retardation times in governing the critical stability thresholds [18]. The effect of vertical throughflow was investigated on thermal convection in an Oldroyd-B fluid saturated bidispersive porous layer, analyzing both the stationary and oscillatory modes of instability [19]. The study revealed that both modes of instability arise in the Oldroyd-B fluid model, whereas only the stationary mode is

observed in the Newtonian fluid model. Further, a modified Darcy-Brinkman Oldroyd B model was employed to examine thermal convection in a porous layer uniformly heated from below [20]. This study demonstrated a significant correlation between the flow resistance offered by the solid matrix and that arising from the Oldroyd-B fluid's viscoelastic behavior which was further corroborated by the study in Ref. [21], rendering Oldroyd-B fluid rheology a robust framework for examining thermal convective instability in a BDPM.

Moreover, the inherent stratification, preferential pore orientation, structural and geometric heterogeneity in a BDPM induces flow pathways that cannot be captured adequately by an isotropic permeability tensor [22]. The intrinsic directional dependence of flow resistance in such hierarchical porous media necessitates the incorporation of anisotropic permeability. In this context, the impact of rotating and anisotropic BDPM on the transition from conduction to thermal convection was investigated, elucidating the critical role of permeability tensor in governing the convective instability [23]. This model was further extended to anisotropic BDPM, employing the Brinkman law to govern flow dynamics in both the macro and micro pore phases [24]. Further, the onset of convection in an anisotropic horizontal bidispersive porous layer saturated with hybrid nanofluid was examined, revealing that the anisotropic permeability ratio significantly alters the stability thresholds of the system [25]. The effect of anisotropy and depth dependent viscosity on the stability of anisotropic BDPM was examined, demonstrating that the interphase momentum transfer coefficient and anisotropic permeability ratio exerts a substantial stabilizing effect on the system [26].

Recently, the onset of thermal convective instability in an Oldroyd-B fluid saturating an anisotropic bidispersive porous layer was investigated [27]. The study employed a modified Darcy Oldroyd model to characterize the viscoelastic flow behavior in both the macro- and micro-pore phases, thereby simultaneously capturing the effects of elastic memory and hierarchical pore-scale structure on the onset of convective instability. However, analyzing only the critical stability thresholds is not enough as it identifies only the transition from conduction to thermal convection without providing any information on the subsequent evolution of the resulting convective structures. To capture the subsequent evolution of system in the vicinity of critical regimes–including the amplitude and heat transport characteristics–it is crucial to investigate the post onset behavior. This also helps in determining whether the system settles into a stable finite-amplitude state or exhibits more intricate dynamical behavior. This constitutes a significant gap in the existing literature, which may largely stem from the huge mathematical complexity of the resulting nonlinear coupled system.

Motivated by this literature gap, the present study investigates weakly nonlinear evolution of thermal convection in an Oldroyd-B fluid saturating an anisotropic bidispersive porous layer. The critical stability thresholds and the evolution of the system in the vicinity of these critical

regimes, along with heat transfer characteristics of the system, are rigorously examined under different parametric conditions. The clear novelty of the present study lies in the incorporation of anisotropic permeability within a viscoelastic bidispersive framework, coupled with a weakly nonlinear stability analysis that, to the best of the authors' knowledge, has not been addressed in the existing literature on Oldroyd-B fluid convection in BDPM. The outcomes of the present study are anticipated to enhance the foundational framework and fundamental understanding of thermal convection in viscoelastic fluids with potential implications spanning across a wide spectrum of thermal, geophysical, and industrial applications.

2. Mathematical Model

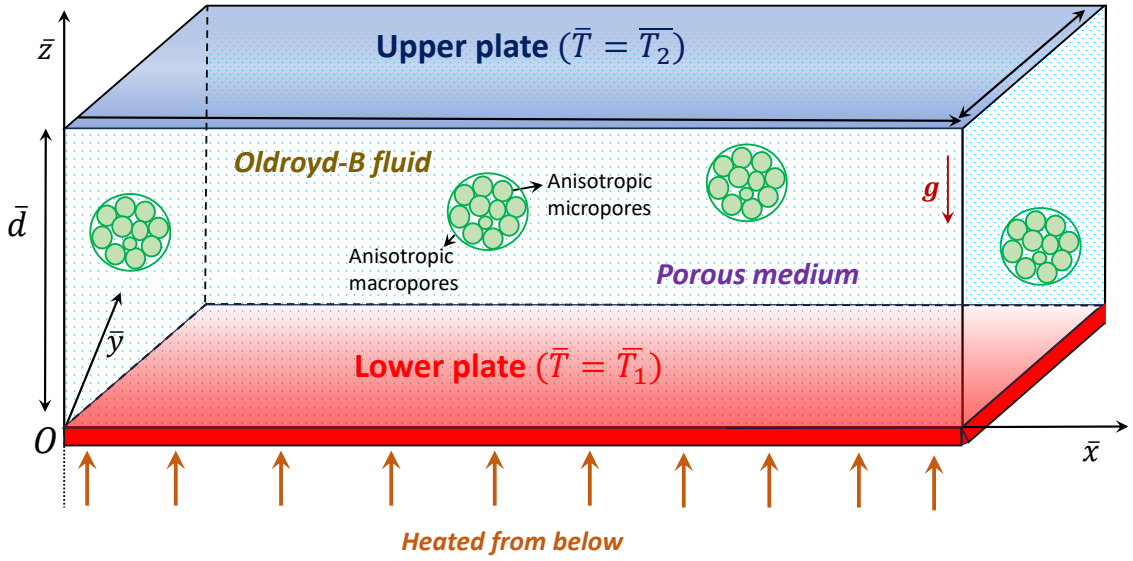


Figure 1: Schematic illustration of a horizontal bidispersive porous layer saturated with an Oldroyd-B fluid, comprising anisotropic micro- and macropore structures.

The current study examines the incompressible, laminar flow of an Oldroyd-B fluid saturating an infinitely long horizontal porous slab of vertical height $\bar{d}$, comprising both relatively small micropores and relatively large macropores, as illustrated in Fig. 1. The horizontal axes are oriented along the $\overline{x}$ and $\overline{y}$ directions, while the $\overline{z}$ axis is oriented vertically upwards, opposite to the direction of gravitational acceleration. The temperature at the lower and upper walls is $\overline{T}_1$ and $\overline{T}_2$, respectively with $\overline{T}_1 > \overline{T}_2$. Additionally, the Oberbeck - Boussinesq approximation [27, 28] is employed, wherein density variations are considered only in the body force term. This approximation, under the assumption of constant pressure, may be expressed as:

$$\overline{\rho} \;=\; \rho_0\big(1 - \alpha(\overline{T} - \overline{T}_2)\big), \tag{1}$$

where, $\overline{\rho}$ signifies density of the fluid, $\overline{T}$ represents temperature, α denotes the thermal expan-

sion coefficient and ρ_0 is the density corresponding to the temperature, $\overline{T}_2$. Building upon this framework, the continuity and momentum equations for an Oldroyd-B fluid flowing through an anisotropic bidispersive porous layer are represented as [27]:

$$\overline{\nabla}\cdot\overline{\mathbf{u}}_f \;=\; 0, \qquad \overline{\nabla}\cdot\overline{\mathbf{u}}_p \;=\; 0, \tag{2}$$

$$\overline{\nabla}\overline{p}_f + \zeta\big(\mathbf{u}_f \;-\; \mathbf{u}_p\big) - \rho_0 g\alpha\big(\overline{T}-\overline{T}_2\big)\mathbf{e}_z \;=\; r_f, \tag{3}$$

$$\overline{\nabla}\overline{p}_p + \zeta\big(\mathbf{u}_p \;-\; \mathbf{u}_f\big) - \rho_0 g\alpha\big(\overline{T}-\overline{T}_2\big)\mathbf{e}_z \;=\; r_p. \tag{4}$$

Here, the subscript f signifies quantities associated with the macropores, while the subscript p denotes those associated with the micropores. Furthermore, $\overline{\mathbf{u}}_f \;=\; (\overline{u}_f, \overline{v}_f, \overline{w}_f)$, and $\overline{\mathbf{u}}_p \;=\; (\overline{u}_p, \overline{v}_p, \overline{w}_p)$ represent the Darcy-scale (volume-averaged) seepage velocities of the macropore and micropore phases, respectively, whereas ζ symbolizes the inter-phase momentum transfer (drag) coefficient that quantifies the momentum exchange between the two phases. The pressures in the macro and micropores are represented by $\overline{p}_f$ and $\overline{p}_p$, respectively. Moreover, the Darcy drag flow resistances due to the solid matrix are quantified by r_f and r_p which are represented as [19, 27]:

$$\left(1+\overline{\lambda}_1\frac{\partial}{\partial\overline{t}}\right)r_f \;=\; -\frac{\mu}{\mathbf{K}_f}\left(1+\overline{\lambda}_2\frac{\partial}{\partial\overline{t}}\right)\overline{\mathbf{u}}_f, \tag{5}$$

$$\left(1+\overline{\lambda}_1\frac{\partial}{\partial\overline{t}}\right)r_p \;=\; -\frac{\mu}{\mathbf{K}_p}\left(1+\overline{\lambda}_2\frac{\partial}{\partial\overline{t}}\right)\overline{\mathbf{u}}_p. \tag{6}$$

In these equations, $\overline{\lambda}_1$ and $\overline{\lambda}_2$ denote the stress relaxation and strain retardation time, respectively, which characterize the viscoelastic memory of the Oldroyd-B fluid, with $\overline{\lambda}_1 \geq \overline{\lambda}_2 \geq 0$ ensuring thermodynamic consistency (positive dissipation) of the constitutive model, $\overline{t}$ denotes time, and μ symbolizes dynamic viscosity of the fluid. Furthermore, $\mathbf{K}_f$ and $\mathbf{K}_p$ represent reciprocal of permeability tensor in the macro- and micropores which are expressed as: $\mathbf{K}_f \;=\; k_{fx}\boldsymbol{i}+k_{fy}\boldsymbol{j}+k_{fz}\boldsymbol{k}$, and $\mathbf{K}_p \;=\; k_{px}\boldsymbol{i}+k_{py}\boldsymbol{j}+k_{pz}\boldsymbol{k}$, respectively. Owing to our restricted focus on horizontal isotropy in the mechanical behavior of porous medium, the permeability tensor is considered to be orthotropic with equal horizontal components, i.e., $k_{fx} = k_{fy}$, and $k_{px} = k_{py}$. Moreover, under the assumption of local thermal equilibrium between the phases, the energy balance equations in the bidispersive porous media are represented as [3, 27]:

$$\big(\rho c\big)_m\frac{\partial\overline{T}}{\partial\overline{t}} \;+\; \big(\rho c\big)_f\big(\overline{\mathbf{u}}_f+\overline{\mathbf{u}}_p\big)\cdot\overline{\nabla T} \;=\; \boldsymbol{\kappa}_m\overline{\nabla}^2\overline{T}. \tag{7}$$

Here, ρc indicates the product of density and specific heat at constant pressure for each corresponding quantity, $\boldsymbol{\kappa}$ denotes thermal diffusivity of the fluid, ϕ_f and ϕ_p signify the ratio of volume occupied by the macropores and micropores, respectively to the total volume of the porous body. Moreover, $\overline{\mathbf{u}}_f = \phi_f\mathbf{V}_f$ and $\overline{\mathbf{u}}_p = \phi_p(1-\phi_f)\mathbf{V}_p$ denote the pore-averaged velocities of the two phases,

where $\mathbf{V}_f$ and $\mathbf{V}_p$ represent the actual fluid velocities within the respective phases. Further,

$$\big(\rho c\big)_m \;=\; (1-\phi_f)(1-\phi_p)\big(\rho c\big)_s \;+\; \phi_f\big(\rho c\big)_f \;+\; \phi_p(1-\phi_f)\big(\rho c\big)_p, \tag{8}$$

$$\boldsymbol{\kappa}_m \;=\; (1-\phi_f)(1-\phi_p)\boldsymbol{\kappa}_s \;+\; \phi_f\boldsymbol{\kappa}_f \;+\; \phi_p(1-\phi_f)\boldsymbol{\kappa}_p, \tag{9}$$

signify effective heat capacity and thermal diffusivity of the medium, respectively, expressed as porosity-weighted combinations of the solid-skeleton, macropore and micropore phases. Here, the subscript s denotes quantities associated with the solid skeleton of the porous matrix, Using $\boldsymbol{\kappa} \;=\; \boldsymbol{\kappa}_m/\big(\rho c\big)_f$, and $\mathcal{M} \;=\; \big(\rho c\big)_f/\big(\rho c\big)_m$ in Eq. (7) yields:

$$\frac{1}{\mathcal{M}}\frac{\partial \overline{T}}{\partial \overline{t}} \;+\; \big(\overline{\mathbf{u}}_f + \overline{\mathbf{u}}_p\big)\cdot\overline{\nabla T} \;=\; \boldsymbol{\kappa}\overline{\nabla}^2\overline{T}. \tag{10}$$

Additionally, applying the no penetration and constant temperature conditions at the upper and lower boundaries yield [27]:

$$\begin{aligned} &\text{at} \quad \overline{z}=0: \qquad \overline{T}=\overline{T}_1, \qquad \overline{w}_f=0, \qquad \overline{w}_p=0,\\ &\text{at} \quad \overline{z}=\overline{d}: \qquad \overline{T}=\overline{T}_2, \qquad \overline{w}_f=0, \qquad \overline{w}_p=0. \end{aligned} \tag{11}$$

Furthermore, the governing equations are transformed into dimensionless form by employing the following scaling parameters [19, 27]:

$$\mathbf{x} \;=\; (x,y,z) \;=\; \frac{1}{\overline{d}}(\overline{x},\overline{y},\overline{z}), \qquad \mathbf{u}_{f,p} \;=\; \frac{\overline{d}}{\boldsymbol{\kappa}}\overline{\mathbf{u}}_{f,p}, \qquad t \;=\; \frac{\boldsymbol{\kappa}}{\overline{d}^2}\overline{t}, \qquad T \;=\; \frac{\overline{T}-\overline{T}_2}{\overline{T}_1-\overline{T}_2},$$

$$p_{f,p} \;=\; \frac{k_{fx}}{\mu\boldsymbol{\kappa}}\overline{p}_{f,p}, \qquad \lambda_1,\lambda_2 \;=\; \frac{\boldsymbol{\kappa}}{\overline{d}^2}\overline{\lambda}_1,\overline{\lambda}_2, \qquad \sigma_f \;=\; \frac{k_{fx}}{\mu}\zeta, \qquad Ra \;=\; \rho_0 g\alpha\frac{\overline{d}k_{fx}}{\mu\boldsymbol{\kappa}}\big(\overline{T}_1-\overline{T}_2\big), \tag{12}$$

where, Ra signifies the Darcy-Rayleigh number. Utilizing Eq. (12), the governing equations (2)–(4)

are represented in the dimensionless form as:

$$\nabla \cdot \mathbf{u}_f = 0, \qquad \nabla \cdot \mathbf{u}_p = 0, \tag{13}$$

$$\left(1+\lambda_1\frac{\partial}{\partial t}\right)\left(\frac{\partial p_f}{\partial x}+\sigma_f(u_f-u_p)\right) + \left(1+\lambda_2\frac{\partial}{\partial t}\right)u_f = 0, \tag{14}$$

$$\left(1+\lambda_1\frac{\partial}{\partial t}\right)\left(\frac{\partial p_f}{\partial y}+\sigma_f(v_f-v_p)\right) + \left(1+\lambda_2\frac{\partial}{\partial t}\right)v_f = 0, \tag{15}$$

$$\left(1+\lambda_1\frac{\partial}{\partial t}\right)\left(\frac{\partial p_f}{\partial z}+\sigma_f(w_f-w_p)-RaT\right) + K_{fr}\left(1+\lambda_2\frac{\partial}{\partial t}\right)w_f = 0, \tag{16}$$

$$\left(1+\lambda_1\frac{\partial}{\partial t}\right)\left(\frac{\partial p_p}{\partial x}+\sigma_f(u_p-u_f)\right) + K_r\left(1+\lambda_2\frac{\partial}{\partial t}\right)u_p = 0, \tag{17}$$

$$\left(1+\lambda_1\frac{\partial}{\partial t}\right)\left(\frac{\partial p_p}{\partial y}+\sigma_f(v_p-v_f)\right) + K_r\left(1+\lambda_2\frac{\partial}{\partial t}\right)v_p = 0, \tag{18}$$

$$\left(1+\lambda_1\frac{\partial}{\partial t}\right)\left(\frac{\partial p_p}{\partial z}+\sigma_f(w_p-w_f)-RaT\right) + K_rK_{pr}\left(1+\lambda_2\frac{\partial}{\partial t}\right)w_p = 0, \tag{19}$$

$$\frac{1}{\mathcal{M}}\frac{\partial T}{\partial t} + (\mathbf{u}_f+\mathbf{u}_p)\cdot\nabla T = \nabla^2 T, \tag{20}$$

where, $K_{fr} = \frac{k_{fx}}{k_{fz}}$, $K_{pr} = \frac{k_{px}}{k_{pz}}$ denote the anisotropy parameters of the macro and micropores, repsectively, $K_r = \frac{k_{fx}}{k_{px}}$ signifies the ratio of macropore to micropore permeability (both evaluated along the x - direction). Analogously, the dimensionless form of boundary conditions specified in Eq. (11) is expressed as:

$$\begin{aligned} &\text{at} \quad z=0: \qquad T=1, \qquad w_f=0, \qquad w_p=0, \\ &\text{at} \quad z=1: \qquad T=0, \qquad w_f=0, \qquad w_p=0. \end{aligned} \tag{21}$$

3. Stability Analysis

This section delineates stability of the system examined by introducing infinitesimal perturbations to the base flow and investigating the behavior of resulting perturbed equations. In this study, the base flow is assumed to be steady, laminar, fully developed and unidirectional characterized by [18, 28]:

$$\mathbf{u}_{f,b}=0, \qquad \mathbf{u}_{p,b}=0, \qquad T_b=T_b(z), \qquad p_b=p_b(z). \tag{22}$$

Here, the subscript b signifies the conduction state. Utilizing these conditions, the basic state temperature profile is obtained by solving Eq. (20) and is expressed as:

$$T_b(z) = 1-z. \tag{23}$$

To analyze the stability of this base flow, each flow variable is decomposed as the sum of its basic state and time dependent perturbation as [10, 19]:

$$\mathbf{u}_f = \mathbf{u}_{f,b} + \mathbf{u}'_f, \qquad \mathbf{u}_p = \mathbf{u}_{p,b} + \mathbf{u}'_p, \qquad p = p_b + p', \qquad T = T_b + T', \tag{24}$$

where $'$ denotes the corresponding perturbed variable. Utilizing these perturbed expressions into the governing equations (13)–(20) and accounting the fact that the base flow satisfies these governing equations, the resulting perturbed equations (omitting the prime notation) are represented as:

$$\frac{\partial u_f}{\partial x} + \frac{\partial v_f}{\partial y} + \frac{\partial w_f}{\partial z} = 0, \qquad \frac{\partial u_p}{\partial x} + \frac{\partial v_p}{\partial y} + \frac{\partial w_p}{\partial z} = 0, \tag{25}$$

$$\left(1 + \lambda_1 \frac{\partial}{\partial t}\right)\left(\frac{\partial p_f}{\partial x} + \sigma_f(u_f - u_p)\right) + \left(1 + \lambda_2 \frac{\partial}{\partial t}\right) u_f = 0, \tag{26}$$

$$\left(1 + \lambda_1 \frac{\partial}{\partial t}\right)\left(\frac{\partial p_f}{\partial y} + \sigma_f(v_f - v_p)\right) + \left(1 + \lambda_2 \frac{\partial}{\partial t}\right) v_f = 0, \tag{27}$$

$$\left(1 + \lambda_1 \frac{\partial}{\partial t}\right)\left(\frac{\partial p_f}{\partial z} + \sigma_f(w_f - w_p) - RaT\right) + K_{fr}\left(1 + \lambda_2 \frac{\partial}{\partial t}\right) w_f = 0, \tag{28}$$

$$\left(1 + \lambda_1 \frac{\partial}{\partial t}\right)\left(\frac{\partial p_p}{\partial x} + \sigma_f(u_p - u_f)\right) + K_r\left(1 + \lambda_2 \frac{\partial}{\partial t}\right) u_p = 0, \tag{29}$$

$$\left(1 + \lambda_1 \frac{\partial}{\partial t}\right)\left(\frac{\partial p_p}{\partial y} + \sigma_f(v_p - v_f)\right) + K_r\left(1 + \lambda_2 \frac{\partial}{\partial t}\right) v_p = 0, \tag{30}$$

$$\left(1 + \lambda_1 \frac{\partial}{\partial t}\right)\left(\frac{\partial p_p}{\partial z} + \sigma_f(w_p - w_f) - RaT\right) + K_r K_{pr}\left(1 + \lambda_2 \frac{\partial}{\partial t}\right) w_p = 0, \tag{31}$$

$$\frac{1}{\mathcal{M}} \frac{\partial T}{\partial t} - (w_f + w_p) + (\mathbf{u}_f + \mathbf{u}_p) \cdot \nabla T = \nabla^2 T. \tag{32}$$

In a similar manner, the corresponding boundary conditions presented in Eq. (21) are represented as:

$$\text{at} \quad z = 0, 1 \qquad T = 0, \qquad w_f = 0, \qquad w_p = 0. \tag{33}$$

Subsequently, a stream-function formulation is introduced, wherein the velocity components are expressed using scalar functions, ψ_f and ψ_p as:

$$u_f = \frac{\partial \psi_f}{\partial z}, \qquad w_f = -\frac{\partial \psi_f}{\partial x}, \qquad u_p = \frac{\partial \psi_p}{\partial z}, \qquad w_p = -\frac{\partial \psi_p}{\partial x}. \tag{34}$$

Utilizing these stream function formulations, Eqs. (25)–(32) are reformulated as:

$$-\left(1+\lambda_2\frac{\partial}{\partial t}\right)\frac{\partial \psi_f}{\partial z} \;+\; \left(1+\lambda_1\frac{\partial}{\partial t}\right)\left(-\frac{\partial p_f}{\partial x}-\sigma_f\left(\frac{\partial \psi_f}{\partial z}-\frac{\partial \psi_p}{\partial z}\right)\right) \;=\; 0, \quad (35)$$

$$K_{fr}\left(1+\lambda_2\frac{\partial}{\partial t}\right)\frac{\partial \psi_f}{\partial x} \;+\; \left(1+\lambda_1\frac{\partial}{\partial t}\right)\left(-\frac{\partial p_f}{\partial z}+\sigma_f\left(\frac{\partial \psi_f}{\partial x}-\frac{\partial \psi_p}{\partial x}\right) \;+\; RaT\right) \;=\; 0, \quad (36)$$

$$-K_r\left(1+\lambda_2\frac{\partial}{\partial t}\right)\frac{\partial \psi_p}{\partial z} \;+\; \left(1+\lambda_1\frac{\partial}{\partial t}\right)\left(-\frac{\partial p_p}{\partial x}-\sigma_f\left(\frac{\partial \psi_p}{\partial z}-\frac{\partial \psi_f}{\partial z}\right)\right) \;=\; 0, \quad (37)$$

$$K_rK_{pr}\left(1+\lambda_2\frac{\partial}{\partial t}\right)\frac{\partial \psi_p}{\partial x} \;+\; \left(1+\lambda_1\frac{\partial}{\partial t}\right)\left(-\frac{\partial p_p}{\partial z}+\sigma_f\left(\frac{\partial \psi_p}{\partial x}-\frac{\partial \psi_f}{\partial x}\right) \;+\; RaT\right) \;=\; 0, \quad (38)$$

$$\frac{1}{\mathcal{M}}\frac{\partial T}{\partial t} \;+\; \left(\frac{\partial \psi_f}{\partial x}+\frac{\partial \psi_p}{\partial x}\right) \;+\; \left(\frac{\partial \psi_f}{\partial z}+\frac{\partial \psi_p}{\partial z}\right)\frac{\partial T}{\partial x} \;-\; \left(\frac{\partial \psi_f}{\partial x}+\frac{\partial \psi_p}{\partial x}\right)\frac{\partial T}{\partial z} \;=\; \frac{\partial^2 T}{\partial x^2} \;+\; \frac{\partial^2 T}{\partial z^2}. \quad (39)$$

The corresponding boundary conditions are expressed as:

$$\psi_f \;=\; \psi_p \;=\; T \;=\; 0 \qquad \text{at} \quad z=0,1. \quad (40)$$

Additionally, differentiating Eq. (35) with respect to z and Eq. (36) wrt x, and subtracting the resulting equations eliminates the pressure term, thereby yielding:

$$-\left(1+\lambda_2\frac{\partial}{\partial t}\right)\left(\frac{\partial^2 \psi_f}{\partial z^2}+K_{fr}\frac{\partial^2 \psi_f}{\partial x^2}\right)+\left(1+\lambda_1\frac{\partial}{\partial t}\right)\left(-\sigma_f\left(\frac{\partial^2 \psi_f}{\partial z^2}-\frac{\partial^2 \psi_p}{\partial z^2}+\frac{\partial^2 \psi_f}{\partial x^2}-\frac{\partial^2 \psi_p}{\partial x^2}\right)-Ra\frac{\partial T}{\partial x}\right) \;=\; 0. \quad (41)$$

Analogously, Eqs. (37) and (38) yields:

$$-K_r\left(1+\lambda_2\frac{\partial}{\partial t}\right)\left(\frac{\partial^2 \psi_p}{\partial z^2}+K_{pr}\frac{\partial^2 \psi_p}{\partial x^2}\right)+\left(1+\lambda_1\frac{\partial}{\partial t}\right)\left(-\sigma_f\left(\frac{\partial^2 \psi_p}{\partial z^2}-\frac{\partial^2 \psi_f}{\partial z^2}+\frac{\partial^2 \psi_p}{\partial x^2}-\frac{\partial^2 \psi_f}{\partial x^2}\right)-Ra\frac{\partial T}{\partial x}\right) \;=\; 0. \quad (42)$$

Furthermore, to maintain the finite amplitude and suppress the exponential growth in stationary mode of instability, Eqs. (39), (41) and (42) are rescaled with a slow time variable (τ) as: $\tau \;=\; \epsilon^2 t$ [28]. Subsequently, the resulting equations are represented in the matrix form as:

$$\begin{bmatrix} -\nabla_2^2-\sigma_f\nabla^2 & \sigma_f\nabla^2 & -Ra\frac{\partial}{\partial x} \\ \sigma_f\nabla^2 & -K_r\nabla_3^2-\sigma_f\nabla^2 & -Ra\frac{\partial}{\partial x} \\ \frac{\partial}{\partial x} & \frac{\partial}{\partial x} & -\nabla^2 \end{bmatrix}\begin{bmatrix} \psi_f \\ \psi_p \\ T \end{bmatrix} \;=\; \begin{bmatrix} \mathcal{B}_1 \\ \mathcal{B}_2 \\ \mathcal{B}_3 \end{bmatrix}, \quad (43)$$

where,

$$\begin{aligned}
\mathcal{B}_1 &= \lambda_2\epsilon^2\frac{\partial}{\partial\tau}\big(\nabla_2^2\psi_f\big) + \lambda_1\epsilon^2\frac{\partial}{\partial\tau}\bigg(\sigma_f\nabla^2\big(\psi_f-\psi_p\big)+Ra\frac{\partial T}{\partial x}\bigg),\\
\mathcal{B}_2 &= K_r\lambda_2\epsilon^2\frac{\partial}{\partial\tau}\big(\nabla_3^2\psi_p\big) + \lambda_1\epsilon^2\frac{\partial}{\partial\tau}\bigg(\sigma_f\nabla^2\big(\psi_p-\psi_f\big)+Ra\frac{\partial T}{\partial x}\bigg),\\
\mathcal{B}_3 &= \frac{-1}{\mathcal{M}}\epsilon^2\frac{\partial T}{\partial\tau} + \frac{\partial(\psi_f,T)}{\partial(x,z)} + \frac{\partial(\psi_p,T)}{\partial(x,z)},\\
\nabla_2^2 &= \frac{\partial^2}{\partial z^2} + K_{fr}\frac{\partial^2}{\partial x^2}, \qquad \nabla_3^2 = \frac{\partial^2}{\partial z^2} + K_{pr}\frac{\partial^2}{\partial x^2}.
\end{aligned}$$

Furthermore, following the fundamental framework for examining the weakly nonlinear stability of the system, perturbations are expressed as a power series expansion in a small parameter (ϵ), and the following asymptotic expansions are employed to characterize the behavior of the system in the vicinity of critical stability thresholds [8, 28]:

$$Ra = Ra_c + \epsilon^2 Ra_2 + \epsilon^4 Ra_4 + \cdots, \tag{44}$$

$$\psi_f = \epsilon\psi_{f1} + \epsilon^2\psi_{f2} + \epsilon^3\psi_{f3} + \cdots, \tag{45}$$

$$\psi_p = \epsilon\psi_{p1} + \epsilon^2\psi_{p2} + \epsilon^3\psi_{p3} + \cdots, \tag{46}$$

$$T = \epsilon T_1 + \epsilon^2 T_2 + \epsilon^3 T_3 + \cdots. \tag{47}$$

Here, Ra_c signifies the critical Rayleigh number, representing the stability threshold marking the transition from conduction to convective motion, whereas ϵ quantifies the deviation of the system from the onset of instability. Notably, the odd terms appearing in Eq. (44), namely $Ra_1,\ Ra_3, \cdots$, are identically zero, signifying contributions that are anti-symmetric in nature and are not sustained by the base state. Thereafter, the perturbation equations are solved systematically for various orders of ϵ.

3.1. First order system analysis

Considering only $\mathcal{O}(\epsilon)$ terms in Eq. (43), the system reduces to a linear formulation with minimal nonlinear effects, retaining only the leading-order dynamics. This system is represented in the matrix form as:

$$\begin{bmatrix} -\nabla_2^2-\sigma_f\nabla^2 & \sigma_f\nabla^2 & -Ra_c\frac{\partial}{\partial x} \\ \sigma_f\nabla^2 & -K_r\nabla_3^2-\sigma_f\nabla^2 & -Ra_c\frac{\partial}{\partial x} \\ \frac{\partial}{\partial x} & \frac{\partial}{\partial x} & -\nabla^2 \end{bmatrix} \begin{bmatrix} \psi_{f1} \\ \psi_{p1} \\ T_1 \end{bmatrix} = \begin{bmatrix} 0 \\ 0 \\ 0 \end{bmatrix}. \tag{48}$$

The solution of this linear system, under the boundary conditions mentioned in Eq. (40), is expressed as [8, 28]:

$$\begin{aligned} \psi_{f1} &= \mathcal{A}_1\ sin(a_c x)\ sin(\pi z), \\ \psi_{p1} &= \mathcal{A}_2\ sin(a_c x)\ sin(\pi z), \\ T_1 &= \mathcal{A}_3\ cos(a_c x)\ sin(\pi z), \end{aligned} \tag{49}$$

where, a_c denotes the critical horizontal wavenumber. Combining Eqs. (48) and (49) yields the expression for critical Rayleigh number, which is expressed as:

$$Ra_c = \delta^2\left(\frac{K_r\delta_2^2\delta_3^2 + \sigma_f\delta^2\left(\delta_2^2 + K_r\delta_3^2\right)}{4a_c^2\sigma_f\delta^2 + \left(\delta_2^2 + K_r\delta_3^2\right)a_c^2}\right), \tag{50}$$

where, $\delta^2 = \pi^2 + a_c^2$, $\delta_2^2 = \pi^2 + K_{fr}a_c^2$, $\delta_3^2 = \pi^2 + K_{pr}a_c^2$. This critical Rayleigh governs the onset of convective instability in a BDPM and aligns well with the corresponding expression obtained from linear stability analysis [27], thereby confirming the reliability and physical fidelity of the present formulation. Moreover, in the absence of anisotropy, i.e. $K_{fr} = K_{pr} = 1$, this expression for critical Rayleigh number is in complete agreement with the expressions reported in Refs. [8, 10]. Furthermore, in this reduced formulation, if we take homogeneous monodisperse porous configuration, i.e. $\sigma_f = 0$, the obtained expression recovers the classical result for monodisperse porous medium, reported in Ref. [4].

3.2. Second order system analysis

Retaining only the $\mathcal{O}(\epsilon^2)$ terms in the system given by Eq. (43) yields the matrix formulation for the second order system analysis which is expressed as:

$$\begin{bmatrix} -\nabla_2^2 - \sigma_f\nabla^2 & \sigma_f\nabla^2 & -Ra_c\frac{\partial}{\partial x} \\ \sigma_f\nabla^2 & -K_r\nabla_3^2 - \sigma_f\nabla^2 & -Ra_c\frac{\partial}{\partial x} \\ \frac{\partial}{\partial x} & \frac{\partial}{\partial x} & -\nabla^2 \end{bmatrix} \begin{bmatrix} \psi_{f2} \\ \psi_{p2} \\ T_2 \end{bmatrix} = \begin{bmatrix} 0 \\ 0 \\ \frac{\partial(\psi_{f1},T_1)}{\partial(x,z)} + \frac{\partial(\psi_{p1},T_1)}{\partial(x,z)} \end{bmatrix}, \tag{51}$$

where, the expressions for ψ_{f1}, ψ_{p1} and T_1 are obtained directly from Eq. (49). Under the boundary conditions specified in Eq. (40), the solutions of second order system are represented as [8, 28]:

$$\psi_{f2} = 0, \qquad \psi_{p2} = 0, \qquad T_2 = \frac{a_c}{8\pi}\Pi_1\Pi_2\mathcal{A}_1^2\ sin(2\pi z), \tag{52}$$

where, $\Pi_1 = 1 + \frac{2\sigma_f\delta^2+\delta_2^2}{2\sigma_f\delta^2+K_r\delta_3^2}$, and $\Pi_2 = -\frac{a_c}{\delta^2}\left(\frac{4\sigma_f\delta^2 + K_r\delta_3^2 + \delta_2^2}{2\sigma_f\delta^2 + K_r\delta_3^2}\right)$. Furthermore, to quantify the heat transfer within the system, the Nusselt number (Nu) is computed as [8, 28]:

$$Nu(\tau) = 1 + \frac{\left[\frac{a_c}{2\pi}\int_0^{2\pi/a_c}\left(\frac{\partial T_2}{\partial z}\right)dx\right]_{z=0}}{\left[\frac{a_c}{2\pi}\int_0^{2\pi/a_c}\left(\frac{\partial T_b}{\partial z}\right)dx\right]_{z=0}}, \tag{53}$$

which is further expressed as:

$$Nu(\tau) = 1 + \Pi_1\Pi_2\frac{a_c}{4}\mathcal{A}_1^2(\tau). \tag{54}$$

In the absence of anisotropy, i.e., $K_{fr} = K_{pr} = 1$, the obtained expression for $Nu(\tau)$ is in complete agreement with that reported in Ref. [8]. Notably, only the analytical form of the expression is recovered under the isotropic permeability limit; quantitative agreement with the reference values additionally requires reduction to the Newtonian fluid limit, since Nu depends on the finite amplitude parameter ($\mathcal{A}_1$), which in turn depends on the relaxation and retardation time parameters (λ_1, and λ_2, respectively) associated with the Oldroyd B fluid.

Additionally, the mean Nusselt number ($\overline{Nu}$) is defined in the interval (0, 2π) which is computed as [28]:

$$\overline{Nu} = \frac{1}{2\pi}\int_0^{2\pi} Nu(\tau)d\tau. \tag{55}$$

3.3. Third order system analysis

The matrix representation of the third order system is formulated by retaining only the $\mathcal{O}(\epsilon^3)$ terms in Eq. (43) and is represented as:

$$\begin{bmatrix} -\nabla_2^2 - \sigma_f\nabla^2 & \sigma_f\nabla^2 & -Ra_c\frac{\partial}{\partial x} \\ \sigma_f\nabla^2 & -K_r\nabla_3^2 - \sigma_f\nabla^2 & -Ra_c\frac{\partial}{\partial x} \\ \frac{\partial}{\partial x} & \frac{\partial}{\partial x} & -\nabla^2 \end{bmatrix}\begin{bmatrix} \psi_{f3} \\ \psi_{p3} \\ T_3 \end{bmatrix} = \begin{bmatrix} \mathcal{N}_{31} \\ \mathcal{N}_{32} \\ \mathcal{N}_{33} \end{bmatrix}, \tag{56}$$

where,

$$\mathcal{N}_{31} = \left(-\lambda_2\delta_2^2\frac{\partial\mathcal{A}_1}{\partial\tau} + \lambda_1\frac{\partial\mathcal{A}_1}{\partial\tau}\left(\sigma_f\delta^2(-2+\Pi_1) - a_cRa_c\Pi_2\right) - Ra_2a_c\Pi_2\mathcal{A}_1\right)\sin(a_cx)\sin(\pi z),$$

$$\mathcal{N}_{32} = \left(\left(K_r\lambda_2\delta_3^2(\Pi_1 - 1) + \lambda_1\left(\sigma_f\delta^2(2-\Pi_1) - a_cRa_c\Pi_2\right)\right)\frac{\partial\mathcal{A}_1}{\partial\tau} - Ra_2a_c\Pi_2\mathcal{A}_1\right)\sin(a_cx)\sin(\pi z),$$

$$\mathcal{N}_{33} = \left(\frac{1}{\mathcal{M}}\Pi_2\frac{\partial\mathcal{A}_1}{\partial\tau} + \frac{a_c^2}{4}\Pi_1\Pi_2\cos(2\pi z)\mathcal{A}_1^3\right)\cos(a_cx)\sin(\pi z).$$

Furthermore, by enforcing the solvability condition, the Ginzburg-Landau (GL) equation governing the stationary convective mode with time-periodic coefficients is derived using

$$\int_{z=0}^{z=1}\int_{x=0}^{x=2\pi/a_c}\left(\psi_{f1}^{*}\mathcal{N}_{31} \;+\; \psi_{p1}^{*}\mathcal{N}_{32} \;+\; T_1^{*}\mathcal{N}_{33}\right)dx\;dz \;=\; 0, \tag{57}$$

where, ψ_{f1}^{*}, ψ_{p1}^{*}, and T_1^{*} are determined by taking adjoint of the matrix obtained in first order system analysis. Consequently, the amplitude evolution is governed by the cubic GL equation of the form [28]:

$$\mathcal{P}_1\frac{\partial \mathcal{A}_1}{\partial \tau} \;=\; \mathcal{P}_2\mathcal{A}_1 \;+\; \mathcal{P}_3\mathcal{A}_1^3. \tag{58}$$

We have not explicitly provided the analytical expressions of $\mathcal{P}_1$, $\mathcal{P}_2$, and $\mathcal{P}_3$ appearing in this equation as they possess extensive algebraic complexity. Notably, the amplitude equation represented in Eq. (58) exhibits non-autonomous behavior. Consequently, its numerical solution is computed using the fourth-order Runge-Kutta (RK-4) technique, subject to the initial condition $\mathcal{A}_1(\tau) \;=\; \mathcal{A}_0$ at $\tau \;=\; 0$ [28]. Moreover, emphasizing the nonlinear dynamics near the onset of instability, we consider the approximation $Ra_2 \approx Ra_c$ [8].

4. Results and Discussions

This section offers a comprehensive graphical analysis of the influence of governing parameters on stability of the system. The variations in critical stability thresholds alongwith the behavior of the system in the vicinity of critical regimes is systematically examined. Furthermore, the heat transfer characteristics, quantified through the Nusselt number, are investigated under different parametric conditions. The resulting trends are analyzed comprehensively alongwith a detailed discussion of the underlying physical mechanisms. Unless explicitly mentioned in a particular graph, the governing parameters are assigned the following default values: $K_r = 100, K_{fr} = 1, K_{pr} = 1, \sigma_f = 0.01, \lambda_1 = 0.7, \lambda_2 = 0.1$.

The impact of governing parameters on the neutral stability curves, emphasizing their influence on the onset of convective instability is illustrated in Fig. 2. It is evident from Fig. 2a that the system's stability increases monotonically by increasing ratio of permeability in the macro and micropore phases with the critical stability threshold (Ra_c) rising from 33.07 at $Kr = 5$ to approximately 39.47 at $K_r = 100$. This behavior is consistent with the findings reported in Ref. [14] and is physically attributable to the reduced micropore permeability, which inhibits fluid motion within the micropores, thereby delaying convective instability and enhancing the stability of the system.

Furthermore, the impact of macropore permeability ratio (K_{fr}) on the critical stability threshold is illustrated in Fig. 2b. It is observed that the onset of convective instability gets markedly delayed with increasing dominance of horizontal permeability over vertical permeability, with Ra_c

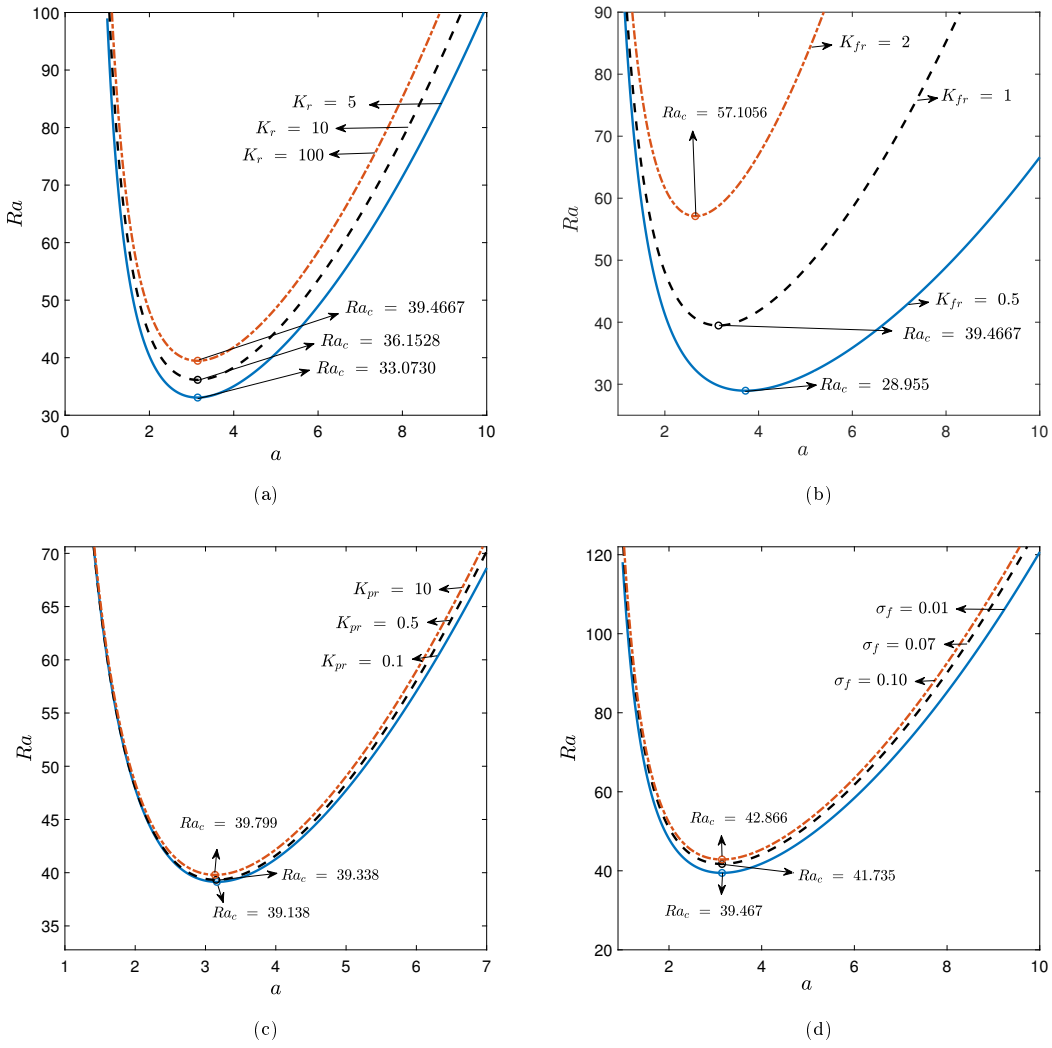


Figure 2: Neutral stability curves illustrating the impact of various governing parameters on the critical stability thresholds.

exhibiting a substantial rise from 28.955 at $K_{fr} = 0.5$ to 57.1056 at $K_{fr} = 2$. Physically, a higher value of K_{fr} indicates a macropore structure that facilitates horizontal fluid motion relative to vertical motion. Since, convective instability is fundamentally driven by vertical fluid transport, a comparatively lower vertical permeability restricts this motion, thereby delaying the onset of convection and enhancing the overall stability of the system. On the other hand, for $K_{fr} < 1$ (i.e., vertical permeability exceeding horizontal permeability), fluid move more readily in the vertical direction, promoting convective motion and destabilizing the system.

Additionally, to capture the influence of micropore permeability (K_{pr}) on the system's stability, its impact on the neutral stability curves is illustrated in Fig. 2c. Analogous to the behavior of K_{fr}, the system's stability increases with increasing value of K_{pr}. However, as shown in this figure, variations in K_{pr} are found to exert only a marginal influence on convective transport: Ra_c

gets augmented from 39.138 to 39.799 as K_{pr} increases from 0.1 to 10. This behavior suggests that the micropore permeability ratio exerts a relatively weaker influence on the system's stability, with only modest variations in the critical stability thresholds. The observed trend in the neutral stability curves with variations in the micropore permeability ratio is in complete agreement with the findings reported in Ref. [27] for the onset of convective instability in a bidispersive porous medium.

The impact of interphase momentum transfer coefficient (σ_f) on the overall stability characteristics of the system is illustrated in Fig. 2d. It is observed that increasing σ_f from 0.01 to 0.1 raises Ra_c from 39.467 to 42.866, revealing a stabilizing effect on the system. Physically, a higher σ_f indicates stronger momentum coupling between the two phases, which enhances the viscous drag experienced by the fluid as it moves between the macropore and micropore regions. This increased inter-phase resistance impedes the convective motion, thereby delaying the transition from conduction to convective instability and rendering the system comparatively more stable.

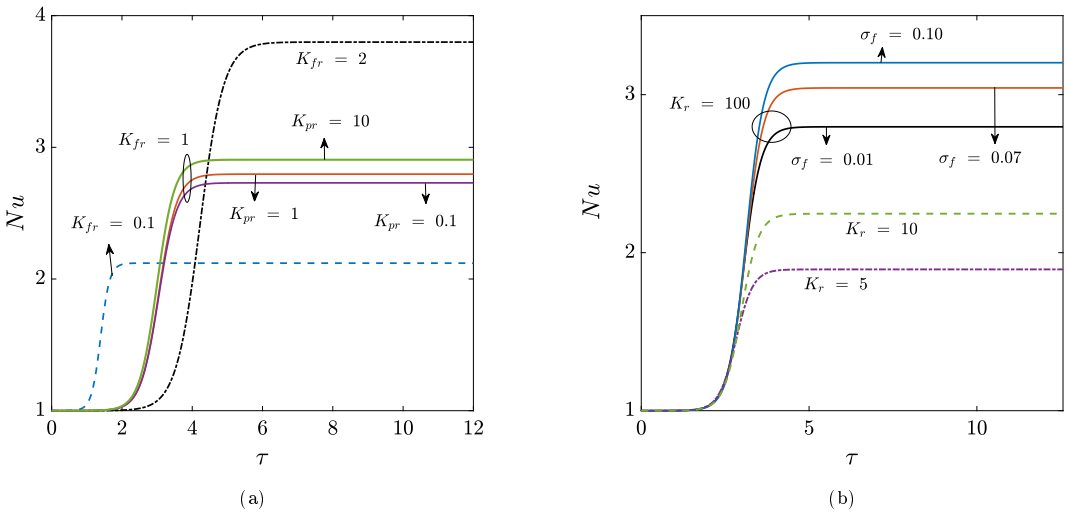


Figure 3: Temporal evolution of the Nusselt number under different parametric regimes.

To characterize the temporal evolution of heat transfer characteristics of the system, Fig. 3 illustrates the variation of the Nusselt number (Nu) under different parametric regimes. In each case, the profiles originate from a conduction-dominated state ($Nu = 1$), followed by a rapid growth phase corresponding to the onset of convection, and eventually attaining a saturated steady state. The impact of macro and micro pore permeability ratio (K_{fr} and K_{pr}, respectively) on the temporal evolution of the Nusselt number is illustrated in Fig. 3a. The value of K_{fr} is systematically varied as 0.1, 1, and 2; indicating a transition from vertically dominating to horizontally dominating permeability. It is observed from this figure that increasing the values of K_{fr} markedly enhances the rate of heat transfer within the system. The saturated Nusselt number exhibits a substantial enhancement with increasing dominance of horizontal permeability over

vertical permeability, indicating intensified nonlinear convective heat transport. However, at the same time, the rise in Nu is shifted towards larger τ, revealing a delayed development of convective cells for higher K_{fr}. Therefore, increasing K_{fr} delays the transient transition toward the convective state but ultimately leads to a considerably stronger heat-transfer regime. The variation in K_{pr} reveals that its influence on the heat-transfer characteristics is comparatively weaker than that of K_{fr}. Increasing K_{pr} from 0.1 to 1, and further to 10, produces only a marginal increase in the saturated Nusselt number, accompanied by a slightly earlier transient transition. This indicates that the micro pore permeability ratio facilitates convective transport to some extent, with its overall contribution to heat-transfer enhancement remaining comparatively weaker relative to that of K_{fr}.

Furthermore, the temporal evolution of the Nusselt number with varying interphase momentum transfer coefficient (σ_f) and the ratio of macropore to micropore permeability (K_r) is illustrated in Fig. 3b. It is evident that the saturated Nusselt number gets augmented with increasing value of σ_f. Physically, a larger σ_f signifies stronger momentum exchange between the macro- and micropore phases, promoting greater dynamical coupling between the two pore networks. This enhanced interphase interaction facilitates the development of convective motion and consequently strengthens the heat transported by convection, leading to a higher asymptotic Nu. The variation in K_r reveals a substantial increase in the saturated Nusselt number as the macropore permeability becomes increasingly dominant over the micropore permeability. This behavior demonstrates that the relative permeability of the two pore networks plays a significant role in governing the intensity of the developed convective state and, consequently, the associated heat transfer.

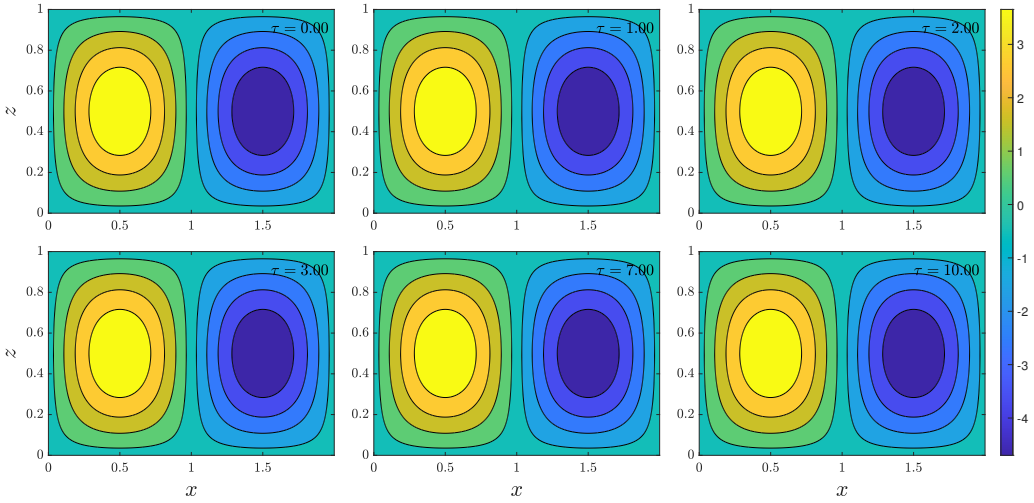
Additionally, to quantify the time-averaged influence of various governing parameters on heat transfer characteristics of the system, its impact on the mean Nusselt number ($\overline{Nu}$) is presented in Table 1. Unless otherwise specified, the parameters are retained at their preceding values. It is observed from this table that increasing the macropore permeability ratio (K_{fr}) augments the heat transfer rate in the post critical regime, revealing that the directional distribution of macropore permeability plays a significant role in regulating post-critical convective heat transport. The transition from $K_{fr} < 1$ to $K_{fr} > 1$ corresponds to a shift from vertically dominated to horizontally dominated permeability, demonstrating a progressive enhancement of the overall heat-transfer rate within the system. In particular, the anisotropic permeability ratio exerts a considerable influence on the saturated disturbance amplitude. Since the convective contribution to the Nusselt number scales with the square of this amplitude, the resulting variation in the nonlinear equilibrium state directly modulates the overall rate of heat transfer. Analogous to the behavior of K_{fr}, the micropore permeability ratio (K_{pr}) is also found to contribute to an enhanced rate of heat transfer within the system by promoting stronger convective circulation and hence a higher $\overline{Nu}$. Further, a rising K_r which signifies an increased dominance of the macropore permeability relative to the

Table 1: Impact of governing parameters on the time-averaged heat transfer characteristics of the system, quantified via the mean Nusselt number ($\overline{Nu}$).

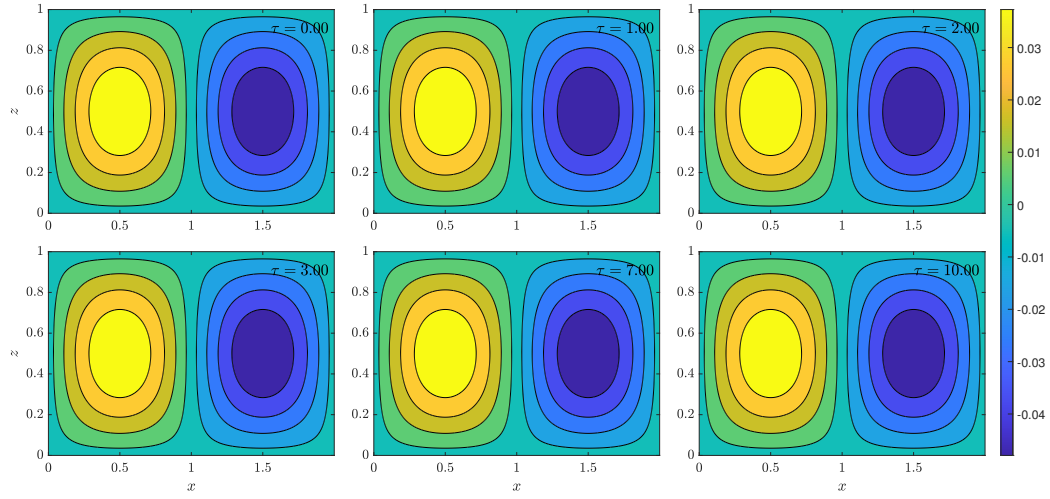
K_{fr}	K_{pr}	K_r	σ_f	λ_1	λ_2	$\overline{Nu}$
0.5	1	100	0.01	0.7	0.1	1.80864
1						1.92402
2						1.96329
1	0.1					1.89163
	1					1.92402
	10					1.98609
	1	5				1.48079
		10				1.67114
		50				1.89298
		100	0.01			1.92402
			0.07			2.04289
			0.10			2.10507
			0.01			1.92402
				0.8		1.65709
				0.9		1.39417
				0.7	0.2	1.91946
					0.3	1.91489
					0.4	1.91034

micropore phase, is found to significantly enhance the heat-transfer rate of the system. Physically, as K_r increases, the macropore network offers progressively less resistance to horizontal flow relative to the micropore phase, channeling convective circulation through the fracture pathway, and thereby strengthening the overall rate of heat transfer within the system. Moreover, the variation in interphase momentum transfer coefficient (σ_f) signifies that increasing value of σ_f augments the heat transfer rate of the system. This behavior is physically attributable to the fact that increasing σ_f strengthens the interphase momentum exchange and fundamentally alters the relative velocity between the macro- and micro-pore phases. This enhanced coupling augments the buoyancy driven convective circulation, thereby rising the mean Nusselt number. Further, at a fixed retardation parameter (λ_2), increasing the relaxation parameter (λ_1) is found to reduce the mean Nusselt number, revealing that enhanced elastic memory suppresses the efficiency of post-critical convective heat transport. Moreover, it is evident that, at a fixed λ_1, increasing λ_2 leads to a modest reduction in the mean Nusselt number. This behavior suggests that the enhanced retardation of the fluid response slightly suppresses the nonlinear convective transport and thereby reduces the

overall heat-transfer efficiency.



(a)



(b)

Figure 4: Streamline contours illustrating the temporal evolution of flow field over slow time for **(a)** macropore and **(b)** micropore phases.

To capture the temporal evolution of flow field over slow time scale (τ), streamline contours for the macropore and micropore phases are illustrated in Figs. 4a and 4b, respectively. The contours are shown at increasing time levels ($\tau = 0, 1, 2, 3, 7$ and 10) to demonstrate the progressive development of flow structures over time. Fundamentally, the flow is characterized by the formation of convection cells, exhibiting symmetric, rotating patterns observed within the domain. Moreover, the persistence of these cells over time indicates the establishment of well formulated and stabilized convective flow patterns.

Furthermore, Fig. 5 illustrates the temporal evolution of isotherm contours over the slow

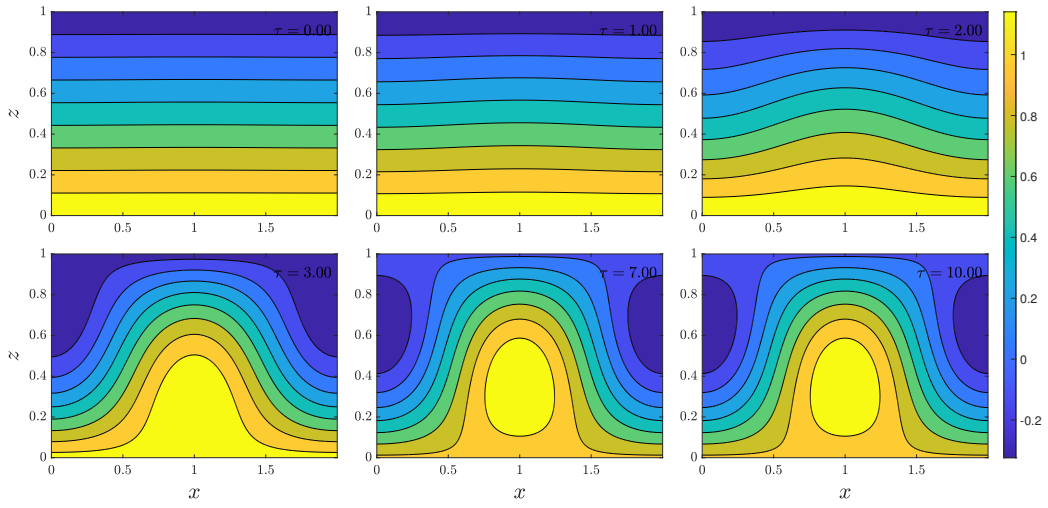


Figure 5: Isotherm contours illustrating the temporal evolution of temperature field over slow time.

time scale (τ), shown at increasing time levels ($\tau = 0, 1, 2, 3, 7$, and 10) to capture the gradual evolution of temperature field. At the initial time ($\tau = 0$), the system exhibits purely conductive temperature distribution, characterized by the horizontal and uniformly spaced isotherms. As the time progresses ($\tau = 2$), isotherms begin to bend significantly, marking the onset of convective motion. Further, at $\tau = 3$, more distorted curves are observed, revealing increasingly prominent and well-developed convective structures. Subsequently, a well defined central thermal plume emerges at $\tau = 7$, indicating a convection-dominated regime in which buoyancy-driven flow substantially distorts the conductive profile. Finally, at large time ($\tau = 10$), the isotherms exhibit fully developed convective cells with highly distorted contours, reflecting strong thermal gradients and efficient heat transport within the system.

Additionally, to gain a deeper insight into the impact of anisotropic permeability on the system's stability relative to the isotropic condition, the critical stability thresholds are examined under various configurations using:

$$\Delta Ra_c = \frac{Ra_c^{\text{configuration}} - Ra_c^{\text{isotropic}}}{Ra_c^{\text{isotropic}}} \times 100.$$

As shown in Table 2, the macro and micro-pore anisotropic configuration exerts a substantial influence on the convective instability of the system by raising the critical Rayleigh number by approximately 330.26% relative to the isotropic case, whereas micro-pore anisotropy alone augments it by only 0.84%. The pronounced percentage variation in the critical stability threshold between the isotropic and anisotropic configurations underscores the physical significance of incorporating directional permeability effects, with the anisotropic porous structures exhibiting markedly enhanced resistance to the onset of convection. To further corroborate the influence of directional

dependence of permeability on the onset of convection, neutral stability curves are examined over a range of interphase momentum transfer coefficient. As illustrated in Fig. 6, the incorporation of anisotropic permeability consistently shifts the neutral stability curves toward higher Rayleigh numbers relative to the isotropic configuration, indicating a delayed onset of convective instability. This behavior persists across the entire range of interphase momentum coupling, thereby reinforcing the stabilizing role of anisotropic permeability in the system.

Moreover, to provide a comparative assessment of the temporal evolution of heat transfer in the Oldroyd-B fluid relative to its Newtonian limit, Fig. 7 illustrates the variation of the Nusselt number with slow time variable (τ) for both fluid configurations, thereby elucidating the influence of viscoelastic rheology on the transient heat transfer characteristics of the system. It is observed from this figure that the Oldroyd-B fluid exhibits an earlier and considerably sharper transition towards the convective regime, followed by rapid attainment of a steady-state value. On the contrary, the Newtonian fluid displays a delayed and more gradual increase in the Nusselt number, indicating a slower development of convective heat transport. Furthermore, the higher asymptotic Nusselt number attained by the Oldroyd-B fluid indicates enhanced heat transfer relative to its Newtonian counterpart, revealing that the viscoelastic effects associated with the Oldroyd-B fluid significantly influence both the transient development and the eventual magnitude of convective heat transfer. Additionally, the mean Nusselt number ($\overline{Nu}$), computed using Eq. (55), is found to be 4.7205 for the Oldroyd-B fluid and 3.2420 for the Newtonian fluid, demonstrating a remarkable enhancement of approximately 45.60% in the time-averaged heat transfer rate relative to the Newtonian limit.

Table 2: Impact of directional dependence of permeability on the system's stability relative to the isotropic permeability conditions.

Configuration	K_{fr}	K_{pr}	a_c	Ra_c	ΔRa_c (%)
Isotropic	1	1	3.1416	39.4667	–
Macro-pore anisotropic	10	1	1.8105	166.1499	320.98
Micro-pore anisotropic	1	10	3.1392	39.7986	0.84
Macro- and micro-pore anisotropic	10	10	1.7705	169.81	330.26

5. Conclusion

The current study investigates weakly nonlinear evolution of thermal convection in an Oldroyd B fluid saturating a horizontal bidispersive porous layer. Owing to the preferential pore orientation and hierarchical geometric stratification frequently observed in naturally occurring bidispersive porous structures, anisotropic permeability is incorporated in both the macro- and micro-pore phases, while a modified Darcy–Oldroyd model is employed to govern the flow dynamics in each phase. For analyzing the stability of the system, infinitesimal perturbations are

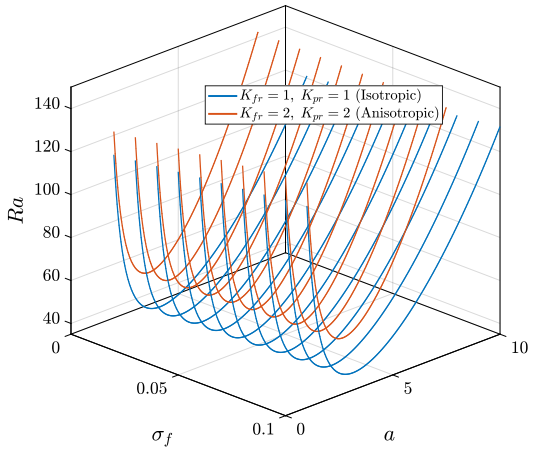


Figure 6: Impact of anisotropic permeability on the convective instability relative to the isotropic configuration across varying strengths of interphase momentum transfer coefficient (σ_f).

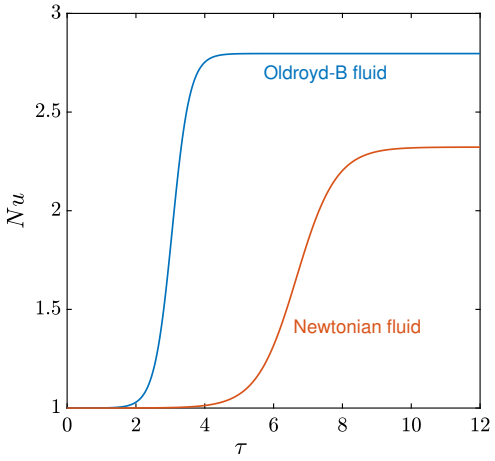


Figure 7: Temporal evolution of the Nusselt number for the Oldroyd-B fluid and its Newtonian limiting case.

superimposed into the base flow and the resulting flow dynamics is systematically investigated under different parametric regimes. Furthermore, to capture both the transition from conduction to thermal convection and the behavior of system in the vicinity of these critical regimes, a finite amplitude Ginzburg-Landau equation is derived via multiple scales expansion. Additionally, to quantify the heat transfer characteristics of the resulting convective structures, the impact of governing parameters on the mean Nusselt number is discussed comprehensively. The key outcomes of the present study are as follows:

- The Oldroyd-B fluid exhibits an earlier and considerably sharper transition towards the convective regime, demonstrating that the viscoelastic memory effects accelerate the transient development of convective heat transport, whereas their absence in the Newtonian limit results in a delayed and more gradual thermal response.

- The directional dependence of permeability in both the macro and micro pore phases raise the critical Rayleigh number by approximately 330.26% relative to the isotropic case, whereas the micro pore anisotropy alone augments it by only 0.84%.

- The time-averaged rate of heat transfer in an anisotropic bidispersive porous layer exhibits a significant enhancement of approximately 45.60% due to the viscoelastic effects associated with the Oldroyd-B fluid rheology, relative to its Newtonian limit.

- The increasing dominance of horizontal permeability over vertical permeability in the macropore phase substantially enhances the stability and heat transfer characteristics of the system, whereas the same trend in the micropore phase yields only a marginal effect.

- Increasing the relaxation time parameter (λ_1) markedly suppresses the mean convective heat

transfer, whereas variations in the retardation time parameter (λ_2) exert only a marginal influence on $\overline{Nu}$, demonstrating that the post-critical heat-transfer response is predominantly governed by the fluid relaxation dynamics.

Overall, the present findings offer deep physical insight into the convective and heat transport behavior of viscoelastic fluids in anisotropic bidispersive porous media, which are widely encountered in the design and control of thermal transport processes across diverse industrial, biological, and geophysical systems, such as enhanced oil recovery, groundwater transport in fractured aquifers, biomedical flows through vascular and tissue networks, and thermal management in polymer-processing operations.

Funding:

Smile Bansal is grateful to the "University Grants Commission (UGC) (1001/(CSIR-UGC NET DEC. 2023))" India for financial assistance to carry out the above research work.

Data availability:

Data sharing is not applicable to this article as no datasets were generated or analysed during the current study.

Conflict of interest:

The authors declare that there are no conflict of interests regarding the publication of this paper.

References

[1] D. Nield, A. Kuznetsov, Heat transfer in bidisperse porous media, in: Transport Phenomena in Porous Media III, Elsevier, 2005, pp. 34–59.

[2] K. Hooman, E. Sauret, M. Dahari, Theoretical modelling of momentum transfer function of bi-disperse porous media, Applied Thermal Engineering 75 (2015) 867–870.

[3] M. Gentile, B. Straughan, Bidispersive thermal convection with relatively large macropores, Journal of Fluid Mechanics 898 (2020) A14.

[4] S. Chandrasekhar, Hydrodynamic and hydromagnetic stability (1960).

[5] D. Nield, A. Kuznetsov, The onset of convection in a bidisperse porous medium, International Journal of Heat and Mass Transfer 49 (17-18) (2006) 3068–3074.

[6] C. Siddabasappa, P. Siddheshwar, S. Mallikarjunaiah, Analytical study of brinkman–bénard convection in a bidisperse porous medium: Linear and weakly nonlinear study, Thermal Science and Engineering Progress 39 (2023) 101696.

[7] B. SM, R. Ragoju, G. Reddy, Effect of viscous dissipation on thermal convection in bidispersive porous media with vertical throughflow: Global stability analysis, Physics of Fluids 36 (8) (2024).

[8] S. Bhavyashree, R. Ragoju, G. S. Reddy, P. Siddheshwar, Soret-driven thermosolutal convection in bidispersive porous medium with vertical throughflow, Physics of Fluids 37 (2) (2025).

[9] A. J. Badday, A. J. Harfash, Thermal convection in rotating bi-disperse porous medium with local thermal nonequilibrium, Heat Transfer 54 (6) (2025) 3723–3737.

[10] M. Gentile, B. Straughan, Bidispersive thermal convection, International Journal of Heat and Mass Transfer 114 (2017) 837–840.

[11] A. J. Badday, A. J. Harfash, Thermosolutal convection in rotating bidispersive porous media with general boundary conditions, Special Topics & Reviews in Porous Media: An International Journal 13 (6) (2022).

[12] S. L. Khalaf, A. J. Harfash, New mathematical methods for convection stability in bidisperse porous media with solute variations, Journal of Engineering Mathematics 151 (1) (2025) 7.

[13] B. A. Jabbar, A. J. Harfash, Double-diffusive convection in bidispersive porous medium with chemical reaction and magnetic field effects, Transport in Porous Media 139 (1) (2021) 45–66.

[14] F. Capone, R. De Luca, M. Gentile, Thermal convection in rotating anisotropic bidispersive porous layers, Mechanics Research Communications 110 (2020) 103601.

[15] K. Pravesh, N. Deepika, Onset of double-diffusive convection in an inclined bidispersive porous layer with magnetic field effect and uniform internal heat source, International Communications in Heat and Mass Transfer 176 (2026) 111313.

[16] S. De, J. Kuipers, E. Peters, J. Padding, Viscoelastic flow simulations in random porous media, Journal of Non-Newtonian Fluid Mechanics 248 (2017) 50–61.

[17] S. Aramideh, P. P. Vlachos, A. M. Ardekani, Nanoparticle dispersion in porous media in viscoelastic polymer solutions, Journal of Non-Newtonian Fluid Mechanics 268 (2019) 75–80.

[18] B. Jia, Y. Jian, Effect of oldroyd-b fluid on thermal convection stability in a bidispersive porous media with relatively large macropores, Physics of Fluids 36 (1) (2024).

[19] B. Jia, Q. Liu, Y. Jian, Thermal convection instability with throughflow in an oldroyd-b fluid saturated bidispersive porous layer, Chinese Journal of Physics 95 (2025) 573–584.

[20] Z. Zhang, C. Fu, W. Tan, Linear and nonlinear stability analyses of thermal convection for oldroyd-b fluids in porous media heated from below, Physics of Fluids 20 (8) (2008).

[21] M. Alishaev, A. K. Mirzadjanzade, For the calculation of delay phenomenon in filtration theory, Izvestya Vuzov, Neft I Gaz 6 (1975) 71–78.

[22] S. Chithram, R. Ragoju, D. Yadav, Effect of anisotropy on the onset of penetrative convection in a bidispersive porous medium, International Communications in Heat and Mass Transfer 175 (2026) 111081.

[23] F. Capone, M. Gentile, G. Massa, The onset of thermal convection in anisotropic and rotating bidisperse porous media, Zeitschrift für angewandte Mathematik und Physik 72 (4) (2021) 169.

[24] F. Capone, R. De Luca, G. Massa, Effect of anisotropy on the onset of convection in rotating bi-disperse brinkman porous media, Acta Mechanica 232 (9) (2021) 3393–3406.

[25] K. Gupta, A. Mahajan, Onset of convection in an anisotropic bidispersive porous media saturated by hybrid nanofluid, Physics of Fluids 38 (6) (2026).

[26] S. Chithram, R. Ragoju, P. Narayana, Stability analysis of an anisotropic bidisperse porous media: The effect of throughflow and depth-dependent viscosity, Physics of Fluids 38 (3) (2026).

[27] B. Jia, Y. Jian, Thermal convection instability in an oldroyd-b fluid saturated anisotropic bidispersive porous layer, International Communications in Heat and Mass Transfer 159 (2024) 108270.

[28] S. Bansal, J. Kaur, S. Sharma, Gravity modulation-induced thermal stability analysis of biviscous bingham fluid saturating a porous medium with uniform internal heat generation, The European Physical Journal Plus 141 (2) (2026) 188.